Nanostructure and magnetic anomaly of mechanosynthesized $Ce_{1-x}Y_xO_{2-\delta}$ ($x \leq 0.3$) solid solutions

Martin Fabián [a,b,*], Dirk Menzel [c], Anatoly Ye Yermakov [d,e,**], Hristo Kolev [f,g], Mária Kaňuchová [f], Jianmin Shi [h], Jaroslav Kováč Jr. [i], Nina Kostova [g], Klebson L. Da Silva [a,j], Mamoru Senna [b,k], Marta Harničárová [l,m], Jan Valíček [l,m], Horst Hahn [b], Vladimír Šepelák [b,m]

[a] *Institute of Geotechnics, Slovak Academy of Sciences, 04001, Košice, Slovakia*
[b] *Institute of Nanotechnology, Karlsruhe Institute of Technology, 76344, Eggenstein-Leopoldshafen, Germany*
[c] *Institute of Condensed Matter Physics, Braunschweig University of Technology, 38106, Braunschweig, Germany*
[d] *M.N. Mikheev Institute of Metal Physics, Ural Branch of the Russian Academy of Sciences, 620137, Yekaterinburg, Russia*
[e] *Institute of Natural Sciences, Ural Federal University, 620083, Yekaterinburg, Russia*
[f] *Faculty of Mining, Ecology, Process Control and Geotechnology, Technical University of Košice, 04001, Košice, Slovakia*
[g] *Institute of Catalysis, Bulgarian Academy of Sciences, 1113, Sofia, Bulgaria*
[h] *Institute of Joining and Welding, Braunschweig University of Technology, 38106, Braunschweig, Germany*
[i] *Institute of Electronics and Photonics, Slovak University of Technology and International Laser Centre, 81219, Bratislava, Slovakia*
[j] *Department of Physics of Materials, State University of Maringá, 87020-900, Maringá, Brazil*
[k] *Faculty of Science and Technology, Keio University, 223-8522, Yokohama, Japan*
[l] *Technical Faculty, Slovak University of Agriculture in Nitra, 94976, Nitra, Slovakia*
[m] *Faculty of Technology, Institute of Technology and Business in České Budějovice, 37001, České Budějovice, Czech Republic*

Keywords:
Ceria-yttria solid solution
Mechanosynthesis
Room-temperature ferromagnetism
Oxygen vacancies

A B S T R A C T

Electromagnetic properties of complex oxide solid solutions containing Ce and Y attract increasing interests due to their high application potential. Their properties are known to be dependent on many factors including grain size and crystal defects. Here we focus on unique features of nanocrystalline $Ce_{1-x}Y_xO_{2-\delta}$ ($x \leq 0.3$) solid solutions prepared via a mechanosynthesis. Mechanically activated $CeO_{2-\delta}$ and mechanosynthesized $Ce_{1-x}Y_xO_{2-\delta}$ exhibit room-temperature ferromagnetism. The saturation magnetization reaches maximum for the $Ce_{0.9}Y_{0.1}O_{2-\delta}$ solid solution. XPS and Raman spectra show that Ce^{4+} ions are partially reduced to Ce^{3+}, with simultaneous introduction of oxygen vacancies accumulated on surface of the solid solutions. An analysis of the experimental magnetization data and the determination of both the spin state and the concentration of magnetic carriers revealed that a small part of the Ce^{3+} spins (<1%) is responsible for the magnetic state of the $Ce_{1-x}Y_xO_{2-\delta}$ system. Existence of clusters with a short-range antiferromagnetic order is also suspected.

1. Introduction

Numerous studies have shown that nanomaterials exhibit functional and structural properties significantly different from those observed for their microcrystalline counterparts. Among others, in recent years, cerium dioxide (ceria, CeO_2) and ceria-based nanomaterials have attracted much attention because they possess many attractive properties which make them highly promising for a wide range of applications such as catalysts, oxygen sensors, solid oxide fuel cells as well as parts of optical, microelectronic and optoelectronic devices [1–7]. The cationic valence balance, Ce^{4+}/Ce^{3+}, is known to significantly influence functional properties of ceria [8]. The room-temperature ferromagnetism (RTFM) in diluted magnetic oxides has attracted considerable interest because of its potential applications for spintronics with room-temperature functionalities. Oxygen vacancies have been proposed to play an important role in the magnetic origin for these oxides [9–11].

It has been reported that crystal defects in insulators with a wide band gap may offer a path to unique ferromagnetic materials [12]. Sundaresan et al. [13] and Ge et al. [14] attributed the RTFM state of

* Corresponding author. Institute of Geotechnics, Slovak Academy of Sciences, 04001, Košice, Slovakia.
** Corresponding author. M.N. Mikheev Institute of Metal Physics, Ural Branch of the Russian Academy of Sciences, 620137, Yekaterinburg, Russia.
E-mail addresses: fabianm@saske.sk (M. Fabián), yermakov@imp.uran.ru (A.Y. Yermakov).

ceria nanoparticles to exchange interactions between unpaired spins that result from surface oxygen vacancies. Also Fernandes et al. [15] reported that the RTFM in nanostructured ceria is mostly associated with point defects, *i.e.*, Ce and O vacancies in the structure. El Hachimi et al. [16] found that oxygen interstitials, oxygen antisites and cerium vacancies in nanocrystalline ceria could induce ferromagnetism. Lu et al. [17] attributed the formation of local magnetic moments mainly to the O_{2p} hole state of the O atoms neighboring the Ce vacancy. On the other hand, Chen et al. [18] and Wang et al. [19] attributed the RTFM in ceria to the existence of net spins. However, some researchers have doubted the effect of oxygen vacancies on the RTFM. For example, Liu et al. [20] observed the RTFM in 20 nm $CeO_{2-\delta}$ powder particles and argued that this phenomenon might not be linked to oxygen vacancies. Li et al. [21] suggested that the RTFM is not related to the surface oxygen vacancies but to the Ce^{3+}/Ce^{4+} pairs. Besides, Lee et al. [22] concluded that RTFM in the ceria solid solution is mainly attributed to Ce^{3+} cations, which accumulate on the particle surface when their concentration increases. Thus, the origin of magnetism and possible mechanisms of its formation in nanostructured ceria-based materials are very complex and not fully understood yet; see, for example, the recent review [23].

In the present work, we report the structure-related magnetic properties of nanocrystalline $Ce_{1-x}Y_xO_{2-\delta}$ ($x \leq 0.3$) solid solutions synthesized via one-step mechanosynthesis. The special effort is devoted to the approximation of the short-range structural arrangement of $Ce_{1-x}Y_xO_{2-\delta}$ via simultaneous use of several analytical methods, *i.e.*, X-ray photoelectron spectroscopy (XPS), diffuse reflectance UV–Vis–NIR and Raman spectroscopies. The observed RTFM is discussed in relationship to the local structure of the mechanosynthesized samples.

2. Experimental

The details of the mechanosynthesis of $Ce_{1-x}Y_xO_{2-\delta}$ ($x \leq 0.3$) solid solutions have been published previously [24]. The XPS measurements were performed using an XPS instrument (SPECS) equipped with PHOIBOS 100 SCD and non-monochromatic X-ray source. The survey surface spectrum was measured at 40 eV at room temperature. All spectra were acquired at a basic pressure of 2×10^{-8} mbar with MgK_α excitation at 10 kV (150 W).

The UV–Vis–NIR diffuse reflectance spectroscopic (DRS) measurements were performed under ambient conditions using a Thermo Evolution 300 UV–Vis–NIR spectrophotometer equipped with a Praying Mantis accessory. The spectra were recorded in the range of 200–1100 nm. The Spectralon (Labsphere, Inc.) as a 'white reflectance standard' was used to collect a background.

The Raman spectra were measured using a MonoVista UV–Vis–NIR confocal Raman Microscope with excitation wavelengths of 514 nm (Ar^+ laser) and 325 nm (He–Cd laser).

Magnetization measurements were performed using a MPMS-5S SQUID magnetometer (Quantum Design). The powder samples were measured in a gelatinous capsule. The magnetization data were corrected for the diamagnetic moment of the capsule.

3. Results and discussion

The detailed information on the X-ray powder diffraction (XRD) analyses and HR-TEM studies of the mechanosynthesized $Ce_{1-x}Y_xO_{2-\delta}$ solid solutions has been presented in our previous work [24]. In brief, the high-energy ball milling of stoichiometric $(1-x)CeO_2:(x/2)Y_2O_3$ mixtures for 90 min resulted in the formation of $Ce_{1-x}Y_xO_{2-\delta}$ ($x \leq 0.3$) solid solutions. Rietveld analysis of XRD data revealed that the crystallite size of the mechanosynthesized powders ranges from 14 to 21 nm and the value of microstrains increases with increasing concentration of Y^{3+} cations. These effects were explained in terms of the formation of oxygen vacancies and replacement of eightfold coordinated Ce^{4+} ions by Y^{3+} or Ce^{3+} ions with different ionic radius. Consequently, it was determined that the lattice parameter a of $Ce_{1-x}Y_xO_{2-\delta}$ decreases linearly with increasing yttrium content up to x 0.2; that is in a good agreement with Vegard's law. However, for $x > 0.2$, a nonlinear behaviour of $a(x)$ was observed. In addition, the determined values of lattice parameters for mechanosynthesized $Ce_{1-x}Y_xO_{2-\delta}$ solid solutions were found to be higher than those of bulk counterparts. The nanoscale character as well as shrinkage of the lattice parameter was further confirmed by HR-TEM analyses. In this context it should be emphasized that the mechanosynthesized $Ce_{1-x}Y_xO_{2-\delta}$ solid solutions are found to be structurally disordered as a result of the following phenomena: (*i*) the onset of the Ce^{4+}/Y^{3+} cation exchange, (*ii*) the reduction of the Ce^{4+}/Ce^{3+}concentration ratio (both followed by the formation of oxygen defects), (*iii*) the presence of a core/shell structure and a high value of surface-to-bulk volume fraction, (*iv*) the accumulation of microstrains. To shed light on the nanostructure of the mechanosynthesized solid solutions on a local atomic scale, in the following we will present and discuss the results obtained comprehensively by several spectroscopic methods. Consequently, on the basis of the results of spectroscopic investigations presented below, we will discuss the origin of the RTFM in the mechanosynthesized solid solutions (parts 3.3 and 3.4).

3.1. Composition and chemical state of mechanosynthesized $Ce_{1-x}Y_xO_{2-\delta}$

The variation in the oxidation state of the cerium ions in the mechanosynthesized $Ce_{1-x}Y_xO_{2-\delta}$ ($x \leq 0.3$) solid solutions manifests itself in their Ce 3d XPS spectra. As shown in Fig. 1, ten sub-peaks were used for the fitting of the Ce 3d spectra; *i.e.*, four peaks (at 881.0, 885.4, 889.4, and 903.8 eV) corresponding to a Ce^{3+} oxidation state and the other six peaks (at 882.4, 888.9, 898.0, 900.8, 907.3, and 916.4 eV) originating from a Ce^{4+} oxidation state [25]. The presence of Ce^{3+} results in the formation of intrinsic defects in the samples and thus partly reflects the concentration of oxygen vacancies. A semiquantitative analysis of the integrated peak area provides information on the concentration of Ce^{3+} ions in the prepared samples. The determined Ce^{3+} fractions in the mechanosynthesized samples are given in Table 1. It should be noted that the mean free path of photoelectrons in ceria oxides for the Ce 3d signal is about 11 nm [26], leading to the value of the information depth of the XPS measurements of about 33 nm (with the approximation that the information depth is three times that of the mean free path of photoelectrons) [27]. Accordingly, taking into account similar values of the information depth and the particle size of the mechanosynthesized $Ce_{1-x}Y_xO_{2-\delta}$ samples ($d_G \sim 14$–21 nm) [24], it could be assumed that the results of XPS measurements reflects not only the surface and interfacial structural disorder (represented by intrinsic defects and oxygen vacancies) but also the interior structure of the prepared nanoparticles.

The ratio between fitted peak areas of Ce^{3+} and Ce^{4+} for ceria can be used to estimate the intrinsic concentration of oxygen vacancies, V_0 (Table 1). According to the F-center exchange mechanism [28], V_0 trapped with one electron can be responsible for an enhanced room-temperature ferromagnetism of the ceria-based materials. However, as shown in Table 1, the mechanosynthesized samples do not show systematic increase of the Ce^{3+} content with increasing yttrium concentration.

3.2. Optical properties and atomic vibrational modes of mechanosynthesized $Ce_{1-x}Y_xO_{2-\delta}$

The UV–Vis–NIR diffuse reflectance spectra of the mechanosynthesized $Ce_{1-x}Y_xO_{2-\delta}$ ($x \leq 0.3$) samples are shown in the inset of Fig. 2. The analysis of the collected experimental data was performed by converting the reflectance spectra to the Kubelka-Munk absorbance spectra (see Fig. 2) using the Kubelka-Munk equation [29].

In the case of CeO_2, band structure calculations show that the valence band (VB) has mainly a 2p(O) character and the conduction band (CB) is essentially of the 5d (Ce) nature. Following the DFT calculations, the gap between these two bands is given to be ~5.75 eV [30].

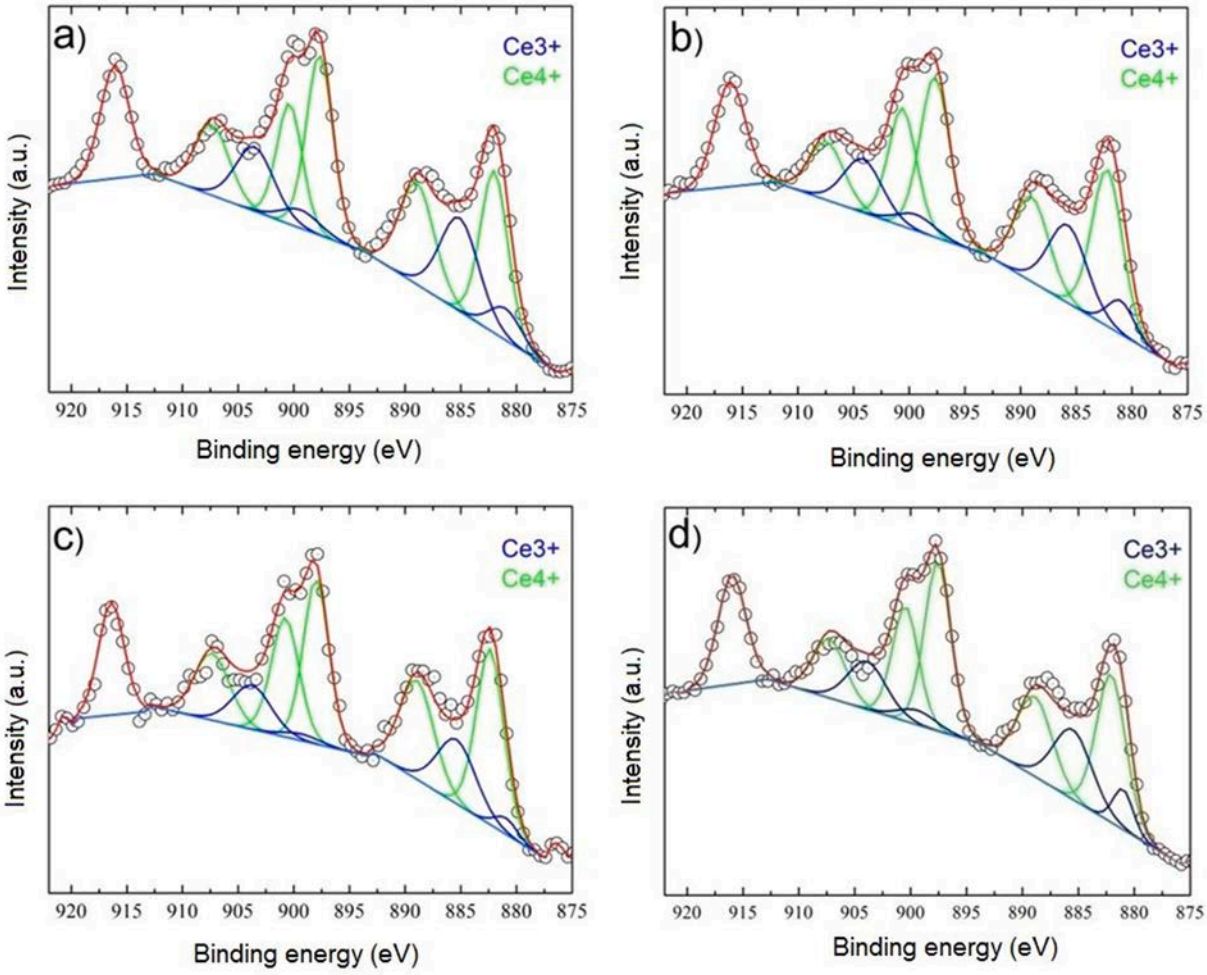

Fig. 1. Experimental data and Gaussian fits of Ce 3d XPS spectra for the mechanosynthesized $Ce_{1-x}Y_xO_{2-\delta}$ with (a) x = 0, (b) x = 0.1, (c) x = 0.2, and (d) x = 0.3.

Table 1
The Ce^{3+} content (at.%) and the crystallite size for the mechanosynthesized $Ce_{1-x}Y_xO_{2-\delta}$ determined by XPS and XRD [24], respectively. Lattice parameters and crystallite size as well as estimated values of direct band gap (E_d) and indirect band gap (E_i), derived from UV–Vis–NIR DRS analyses (presented in part 3.2), are also given.

Nominated Composition	CeO_2-δ (ball milled)	$Ce_{0.9}Y_{0.1}O_{2-\delta}$	$Ce_{0.8}Y_{0.2}O_{2-\delta}$	$Ce_{0.7}Y_{0.3}O_{2-\delta}$
Ce^{3+}(at.%)	27	24	19	23
Composition derived from XPS analysis	$Ce^{IV}_{0\,73}Ce^{III}_{0\,27}O_{1\,865}$	$Ce^{IV}_{0\,684}Ce^{III}_{0\,216}Y_{0\,1}O_{1\,842}$	$Ce^{IV}_{0\,648}Ce^{III}_{0\,152}Y_{0\,2}O_{1\,624}$	$Ce^{IV}_{0\,539}Ce^{III}_{0\,161}Y_{0\,3}O_{1\,4965}$
Lattice parameter, *a* (Å)	5.4231 (1)	5.4189 (9)	5.4153 (9)	5.4101 (2)
Crystallite size (nm)	21	17	17	14
Direct band gap (Ed) (eV)	3.40	3.40	3.38	3.38
Indirect band gap (Ei) (eV)	3.11	3.11	3.09	3.09

However, the 4f-block band that is empty for Ce^{4+} lies between the VB and CB, and the experimental optical gap, *i.e.,* E_g is attributed to a 2p(O) → 4f (Ce) charge transfer [31,32]. As it is clearly seen in Fig. 2, all the samples strongly absorb the UV light below 400 nm (above ~3.1 eV). The optical absorption intensity of the milled $CeO_{2-\delta}$ sample is higher in comparison to its bulk counterpart. Additionally, the absorption intensity decreased with increasing yttrium content, most likely due to the lower values of yttrium refractive index [33]. The band gap energies are determined by fitting the absorption data to the direct/indirect transition equation by extrapolating on the linear portions of the curves to absorption equal to zero (see Fig. S1 in supplementary files), and they are listed in Table 1. The correlated direct band gap (E_d) for ball milled $CeO_{2-\delta}$ nanoparticles (average crystallite size $d_G \sim 21$ nm) was found to be 3.4 eV. This value is within the range characteristic for nanocrystalline $CeO_{2-\delta}$ (3.31–3.7 eV) previously reported in the literature [1,34–38]. Compared to the bulk CeO_2 (E_d 3.10–3.40 eV) [34,35] the ball milled $CeO_{2-\delta}$ samples did not show a significant variation in E_d. Although Liu et al. [39] and Cheviré et al. [31] reported on blue shifting phenomena due to the creation of new (extrinsic) oxygen vacancies upon doping, this effect has not been observed in the prepared samples. Since the conduction and the valence bands are relatively flat according to reported electronic calculations [40], one can assume a direct band gap transition. However, for completeness, the values of the indirect band gaps (E_i) are also included in Table 1. The calculated value for indirect band gap for ball milled $CeO_{2-\delta}$ (3.13 eV) was lower than that of the bulk sample (3.22 eV) and within the E_i range of reported values characteristic for nanocrystalline $CeO_{2-\delta}$ samples (2.41–3.13 eV) [41–45].

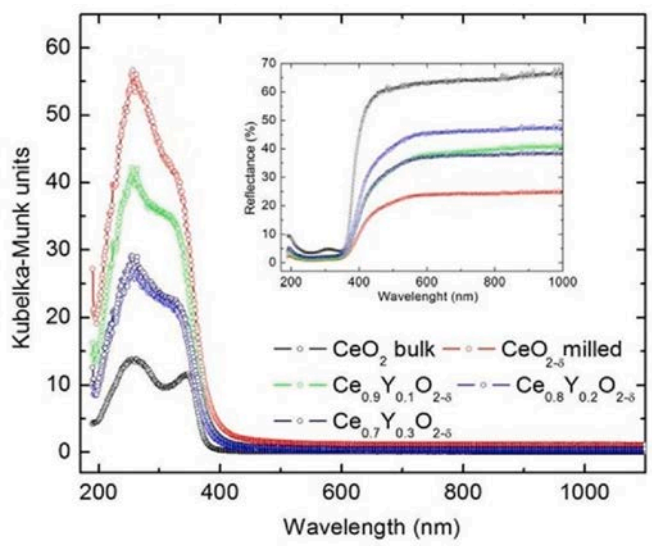

Fig. 2. Room-temperature optical absorbance and reflectance (inset) spectra of the milled $CeO_{2-\delta}$ sample, its bulk counterpart, and of the mechanosynthesized $Ce_{1-x}Y_xO_{2-\delta}$ solid solutions.

In order to better understand the nature of defects induced by ball milling and the charge compensation when yttrium is introduced into ceria Fig. 3 shows Raman spectra of the ball milled $CeO_{2-\delta}$ and of the mechanosynthesized $Ce_{1-x}Y_xO_{2-\delta}$ ($x \leq 0.3$) solid solutions collected under ambient conditions with two different excitation laser lines. As shown in Fig. 3, the spectra are dominated by two bands; besides the F_{2g} mode vibration centered at about 460 cm^{-1} another broad band located at about 600 cm^{-1} is clearly visible. The F_{2g} mode can be understood as symmetrical stretching vibration of the oxygen atoms around cerium ions. The broad band at about 600 cm^{-1} can be explained as a superposition of two subspectra centered at about 560 and 600 cm^{-1}. The band at 560 cm^{-1} is assigned to the extrinsic oxygen vacancies as a result of the charge compensation when Ce^{4+} cations are replaced by trivalent ones. The weak band centered at about 600 cm^{-1} is attributed to the intrinsic oxygen vacancies as a result of the Ce^{4+} to Ce^{3+} reduction [24]. A considerable amount of work has demonstrated that Raman spectral features are significantly influenced by the excitation laser line used. This is due to different penetration depths of electromagnetic radiation [32,46,47]. According to Fig. 2, the mechanosynthesized samples strongly absorb UV light while there is no absorption in the visible range. This demonstrates that the present UV and Vis Raman spectra were measured at the resonant and non-resonant (or weakly resonant) conditions, respectively. The spectra recorded at the 514 nm excitation laser line reflect both the bulk and surface structure due to the weak absorption of the samples, while the spectra measured at 325 nm reflect only the particle surface structure due to the strong UV light absorption of the samples [47,48].

As it is seen in Fig. 3b, when UV laser line is used, the bands at 560 and 600 cm^{-1} merge together and appear as a one broad band, and the band at 460 cm^{-1} is much weaker compared to that measured using a visible laser line. Accordingly, we can conclude that both, the Ce^{4+} to Ce^{3+} reduction as well as the formation of extrinsic and intrinsic oxygen defects in the ball milled $CeO_{2-\delta}$ and in its yttrium containing solid solutions are spatially confined to their surface rather than to inner core of the nanocrystallites.

3.3. *Magnetic properties of $Ce_{1-x}Y_xO_{2-\delta}$ prepared by mechanosynthesis*

The results of dc magnetization measurements performed at RT are shown in Fig. 4. Contributions to the magnetization, which are linearly dependent on the magnetic field, have been substracted from the magnetization data. It is well-known that stoichiometric CeO_2 does not possess ferromagnetic behaviour. Excluding extrinsic nature responsible for magnetism (*e.g.*, 3d-impurities, segregations), several reasons of intrinsic nature of its spontaneous magnetization have been proposed. They include (*i*) oxygen vacancies connected to impurity presence in the gap of the semiconductor accompanied by the realization of the Stoner criterion for ferromagnetism [49] and (*ii*) the exchange interaction between magnetic carriers (*e.g.*, Ce^{3+} having J 5/2) mediated via, *e.g.*, F^+ centres. Theoretical calculations have pointed out that the oxygen vacancies formed on the surface of cerium oxide are more stable than those present in the bulk of the material [50].

We, thus, suppose a structural inhomogeneity within a

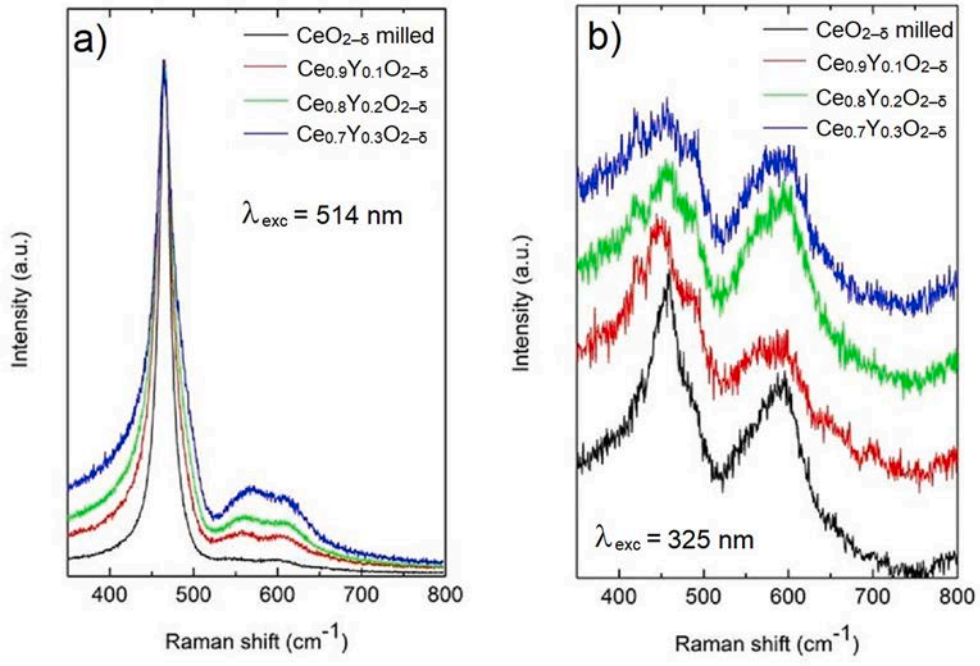

Fig. 3. Raman spectra of the ball milled $CeO_{2-\delta}$ and mechanosynthesized $Ce_{1-x}Y_xO_{2-\delta}$ samples recorded with (left) 514 and (right) 325 nm excitation laser lines.

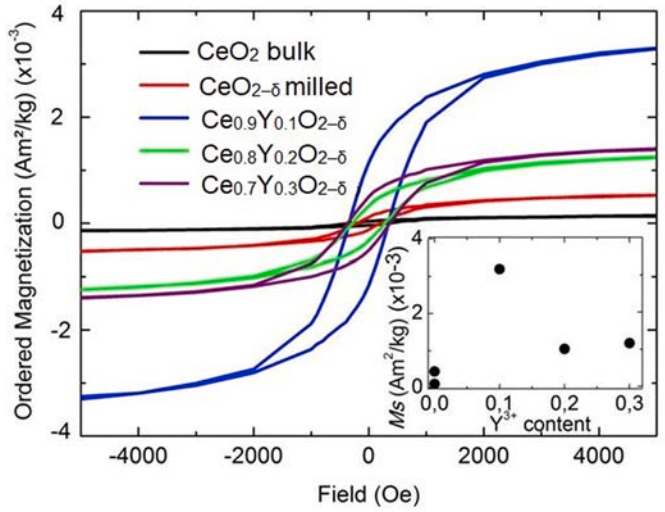

Fig. 4. Room-temperature ordered magnetization of ball milled nanocrystalline $CeO_{2-\delta}$, its bulk counterpart, and of $Ce_{1-x}Y_xO_{2-\delta}$ ($x \leq 0.3$) solid solutions. The inset shows $M_s(x)$ behaviour.

mechanosynthesized solid solution, $Ce_{1-x}Y_xO_{2-\delta}$ with an enhanced concentration of Ce^{3+} and oxygen defects at the near surface region. This is in line with the results of Raman spectroscopic investigations discussed above. It has already been reported that oxygen vacancies in nano-$CeO_{2-\delta}$ tend to migrate to the surface of the nanoparticles [51].

Hence, it should be noted that a high concentration of surface-localized vacancies may fulfill the Stoner criterion [52] due to the formation of an impurity band in the gap. On top of that, the surface of the nanoparticles or grain boundaries may act as an electron donor or acceptor, *i.e.*, the charge transfer can provide magnetism [53,54]. Similar influence can be attributed to the surface-concentrated oxygen/cation vacancy defects in $CeO_{2-\delta}$ structure [55]. However, with respect to complexity of the investigated system the influence of superexchange interactions (usually AF type) and RKKY (Rudermann--Kittel-Kasuya-Yoshida) interactions via delocalized charge carriers on the surface can also not be excluded. As further seen in Fig. 4, when yttrium is introduced into ceria, the saturation magnetization (M_s) reaches its maximum for the sample $Ce_{0.9}Y_{0.1}O_{2-\delta}$ (3.2×10^{-3} Am^2/kg).

3.4. Discussion of magnetic properties of mechanosynthesized $Ce_{1-x}Y_xO_{2-\delta}$

In the following, the magnetization behaviour of the mechanosynthesized $Ce_{1-x}Y_xO_{2-\delta}$ is evaluated using a model of localized carriers (Ce^{3+} ions) of the magnetic moment. According to XPS analyses, the concentration of Ce^{3+} ions (responsible for the formation of both the paramagnetic and ferromagnetic states) is not proportional to the number of introduced yttrium atoms (see Table 2). The estimation of the content of Ce^{3+} carriers, bringing about a ferromagnetic state with a value of about 0.003 Am^2/kg (for the sample with x 0.1), gives a concentration of about 5×10^{-3}. Thus, the concentration of carriers providing the ferromagnetic state is very low ($\leq$1%). Hence, many open questions remain regarding the origin, localization and distribution of the rest of Ce^{3+} magnetic moments in the sample. The shape of the magnetization curves for all the samples in the temperature range from 100 K to 300 K is mainly characterized by a paramagnetic contribution (Figs. S2–S6 in supplementary files). A very small ferromagnetic contribution (0.001–0.002 Am^2/kg) appears for samples $Ce_{1-x}Y_xO_{2-\delta}$ (x 0.2 and 0.3). Analyzing both, the magnetization curves for all the samples and their temperature dependences $\chi T(T)$ in the range of 100–300 K (χ is the susceptibility), we can conclude that the observed room-temperature ferromagnetism is relatively small but of physical significance. As it is seen in Fig. 5, the extrapolated χT dependences have a negative Weiss constant demonstrating that in the mechanosynthesized $Ce_{1-x}Y_xO_{2-\delta}$ the antiferromagnetic contribution is very important.

As shown in Fig. 6, the experimental magnetization curves measured at 5 K are well described by the Brillouin function (small ferromagnetic contribution was extracted), where only the total magnetic moment of the Ce^{3+} ion with the unquenched orbital contribution equal to J L + S 5/2 is used.

As listed in Table 2, from the analysis of the magnetization curves at two temperatures (5 and 100 K) it is possible to estimate the required concentration (x*) of magnetic Ce^{3+} carriers with J 5/2. A satisfactory description of the magnetization curve by the Brillouin function including the bulk state of CeO_2 also indicates that the anisotropic contributions to magnetization can be neglected even for unquenched orbital contributions. This is probably due to the fact that the position of the Ce^{3+} atom in the lattice in the nearest environment is characterized by a quasi-spherical distribution of the crystal field with a relatively small value. In the context of the present paper, it is more appropriate to write chemical formula of the $Ce_{1-x}Y_xO_{2-\delta}$ compounds in the form $Ce_{[1-(x+x^*)]}^{4+}Ce_{x^*}^{3+}Y_xO_{2-\delta}$, taking into account the concentration (x*) of free magnetic Ce^{3+} carriers.

Note that except of the Brillouin function we used an

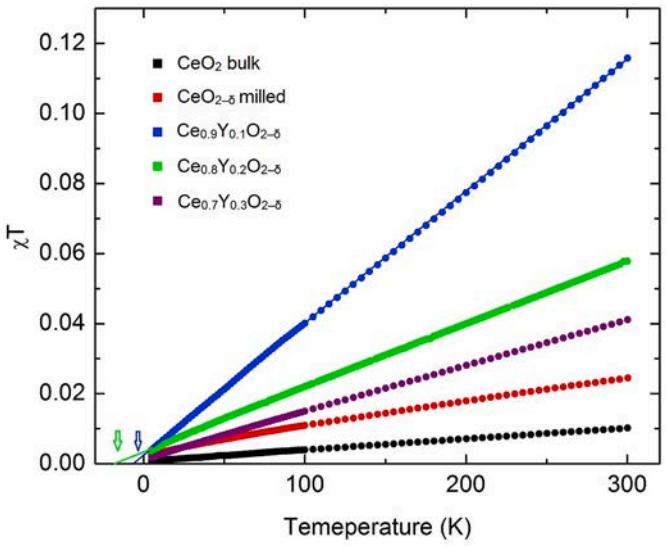

Fig. 5. (χT) *vs.* T for the bulk CeO_2, the milled $CeO_{2-\delta}$ and the mechanosynthesized $Ce_{1-x}Y_xO_{2-\delta}$ ($x \leq 0.3$) solid solutions. The arrows indicate the values of negative extrapolated temperatures θ (6.5 and 19.5 K) for two compounds ($Ce_{0.9}Y_{0.1}O_{2-\delta}$ and $Ce_{0.8}Y_{0.2}O_{2-\delta}$) as examples.

Table 2
The magnetization values and concentrations (x*) of Ce^{3+} spins for $Ce_{[1-(x+x^*)]}^{4+}Ce_{x^*}^{3+}Y_xO_{2-\delta}$ derived from Brillouin functions at 5 K and 100 K.

Nominated composition	CeO_2 bulk	CeO_2-δ milled	$Ce_{0.9}Y_{0.1}O_2$–δ	$Ce_{0.8}Y_{0.2}O_2$–δ	$Ce_{0.7}Y_{0.3}O_2$–δ
Magnetization at 5 K (Am^2/kg)	0.027	0.065	0.07	0.059	0.044
$Ce_{x^*}^{3+}$ (at.%)	0.012	~0.032	0.045	0.035	0.022
Brillouin function (at 5 K)	$2.4 \times 10^{\ 7}H$	$4 \times 10^{\ 7}H$	$1 \times 10^{\ 7}H$	$1 \times 10^{\ 7}H$	$2 \times 10^{\ 7}H$
$Ce_{x^*}^{3+}$ (at.%)	0.012	0.032	0.045	0.015	0.022
Brillouin function (at 100 K)	$1 \times 10^{\ 7}H$	$1.5 \times 10^{\ 7}H$	–	$1 \times 10^{\ 7}H$	$1 \times 10^{\ 7}H$

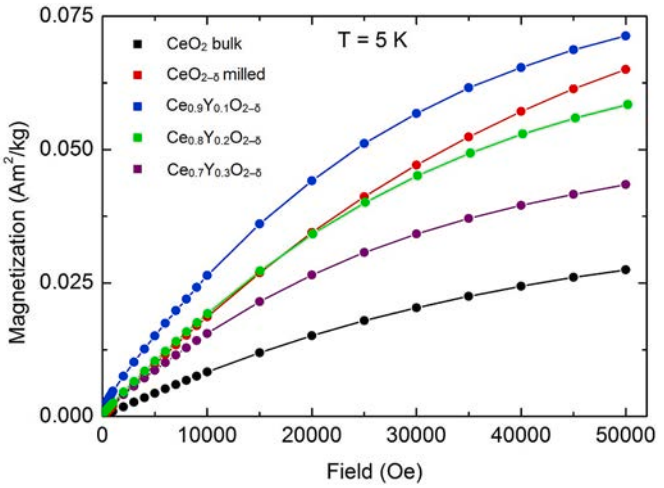

Fig. 6. Experimental magnetization curves for all the investigated samples measured at 5 K (points) and the corresponding Brillouin functions (solid lines). The colours of the points and lines correspond to those described in Fig. 5. The value of the spin in the Brillouin function for Ce^{3+} is J = 5/2. All magnetization curves are satisfactorily described by the Brillouin function using the content of Ce^{3+} which is essentially less than that determined for the corresponding samples by XPS.

antiferromagnetic (AF) contribution in the form of a linear dependence $\chi_{af}H$ (where χ_{af} is antiferromagnetic susceptibility of antiferromagnetic correlations, H is the external magnetic field) to describe in detail the magnetization data of $Ce_{[1-(x+x^*)]}^{4+}Ce_{x^*}^{3+}Y_xO_{2-\delta}$. It is quite a rough calculation but it allows us to estimate the discovered AF contribution in the samples. This suggestion describes the magnetic behaviour of the samples in the defined temperature range quite reasonably. The AF interaction χ_{af} slightly decreases at higher temperatures.

Hence, only very small content of paramagnetic Ce^{3+} spins contribute to the experimental curves described by Brillouin functions. To explain the different content of Ce^{3+} determined by XPS and estimated from magnetic measurements, several physical reasons should be analyzed. Firstly, we can propose the existence of low spin state for Ce^{3+}. However, there is no physical reason to ascribe another spin state for cerium except S 5/2 due to the localized nature of Ce^{3+}. Besides, the attempt to describe magnetization curve by the Brillouin function with a variable concentration and spin values S 1/2, 3/2 and S 2, admitting the existence of a low spin state, was unsuccessful (not shown in the paper). The discrepancy between the Brillouin function and the experimental curve for the milled $CeO_{2-\delta}$ could be attributed to the contamination of the sample by ferromagnetic impurities (sample preparation by ball-milling in Co containing WC container) [24]. Nevertheless, the presence of secondary impurities contribution to explain the Ce^{3+} content discrepancy should be excluded. Accordingly, it seems impossible to completely exclude the formation of antiferromagnetic phases with a crystal structure and long-range magnetic order. These phases, however, would have to be detected. Considering the results of our previous work [24], only solid solutions are formed, which do not contain other extraneous phases. As mentioned above, negative temperatures θ obtained by extrapolation of χT(T) are indicators of negative exchange interactions between Ce^{3+} carriers existing in the system. The number of these regions or magnetic clusters containing Ce^{3+} ions is relatively small, however their volume fraction is much larger than the concentration of free non-interacting carriers described by the Brillouin function. In other words, a significant part of the carriers of the magnetic moment at low and even high temperature can interact with each other antiferromagnetically and, therefore, will not contribute to the macroscopic magnetization. It can also be assumed that the value of the negative exchange interaction between the spins is sufficiently large and, therefore, does not affect the shape of the magnetization curve. The estimation of the Ce^{3+} carrier concentration, which would not participate in the exchange interaction with increasing temperature to 100 K, shows that the number of free carriers remain practically the same.

4. Conclusions

In this paper, structural, optical and magnetic properties of mechanosynthesized $Ce_{1-x}Y_xO_{2-\delta}$ ($x \leq 0.3$) solid solutions are studied. Spectroscopic investigations show that oxygen vacancies are mostly located on the surface of mechanosynthesized particles rather than in their interior. The XPS spectra indicate that the concentration of Ce^{3+} is higher than 19 at.% for all the samples treated by ball-milling. Magnetic measurements show a weak room-temperature ferromagnetism of the ball milled $CeO_{2-\delta}$ and the mechanosynthesized $Ce_{1-x}Y_xO_{2-\delta}$ ($x \leq 0.3$) solid solutions. The magnetization curves at low temperatures of all the compounds are well described by the Brillouin function, assuming the total spin for Ce^{3+} equals to J L + S 5/2 with the unquenched orbital contribution. However, the value of the magnetization is not proportional to the concentration of the added yttrium. The experimental magnetization curves of $Ce_{1-x}Y_xO_{2-\delta}$ are described by the Brillouin function with a free Ce^{3+} magnetic carriers with the concentration of <1 at.%. Moreover, existence of clusters or regions with a short-range antiferromagnetic order was also found.

Author statement

All persons who meet authorship criteria are listed as authors, and all authors confirm that they have participated sufficiently in the work to take public responsibility for the content, including participation in the concept, design, analysis, writing, or revision of the manuscript. Furthermore, each author confirmes that this material or similar material has not been and will not be submitted to or published in any other publication before its appearance in the ***Journal of Physics and Chemistry of Solids***.

Declaration of competing interest

Hereby we confirm, that the corrected version of the manuscript entitled "**Nanostructure and magnetic anomaly of mechanosynthesized $Ce_{1-x}Y_xO_{2-\delta}$ ($x \leq 0.3$) solid solutions**" by *M. Fabián and co-authors* for publication in ***Journal of Physics and Chemistry of Solids*** does not possesses any conflict of interest.

Acknowledgements

The present work is supported by the APVV (project 19-0526), EUREKA (project E!9982) and the VEGA (project 2/0055/19). A. Ye. thanks the State Assignment (Theme *"Magnit"* No. AAAA-A18-118020290129-5) for financial support. H.K., K.L.S. and M.S. are grateful to the National Scholarship Program of Slovakia (SAIA, n. o.). V.Š. acknowledges the support by the DFG (project SE 1407/4-2).

References

[1] S. Phoka, P. Laokul, E. Swatsitang, V. Promarak, S. Seraphin, S. Maensiri, Synthesis, structural and optical properties of CeO_2 nanoparticles synthesized by a simple polyvinyl pyrrolidine (PVP) solution route, Mater. Chem. Phys. 115 (2009) 423–428.

[2] S. Gnanam, V. Rajendran, Synthesis of CeO_2 or α-Mn_2O_3 nanoparticles via sol-gel process and their optical properties, J. Sol. Gel Sci. Technol. 58 (2011) 62–69.

[3] T. Dhannia, S. Jayalekshmi, M.C. Santosh Kumar, T. Prasada, Rao, A. Chandra Bose, Effect of iron doping and annealing on structural and optical properties of cerium oxide nanocrystals, J. Phys. Chem. Solid. 71 (2010) 1020–1025.

[4] M.K. Rath, S.K. Acharya, B.H. Kim, K.T. Lee, B.G. Ahn, Photoluminescence properties of sesquioxide doped ceria synthesized by modified sol-gel route, Mater. Lett. 65 (2011) 955–958.

[5] P. Patsalas, S. Logothetidis, L. Sygellou, S. Kennou, Structure-dependent electronic properties of nanocrystalline cerium oxide films, Phys. Rev. B 68 (2003), 035104.

[6] S. Yabe, T. Sato, Cerium oxide for sunscreen cosmetics, J. Solid State Chem. 171 (2003) 7–11.

[7] L. Truffault, M.T. Ta, T. Devers, K. Konstantinov, V. Harel, C. Simmonard, C. Andrezza, I.P. Nevirkovets, A. Pineau, O. Veron, J.P. Blondeau, Application of nanostructured Ca doped CeO_2 for ultraviolet filtration, Mater. Res. Bull. 45 (2010) 527–535.

[8] S. Tiwari, G. Rathore, N. Patra, A.K. Yadav, D. Bhattacharya, S.N. Jha, C.M. Tseng, S.W. Liu, S. Biring, S. Sen, Oxygen and cerium defects mediated changes in structural, optical and photoluminescence properties of Ni substituted CeO_2, J. Alloys Compd. 782 (2019) 689–698.

[9] J.M.D. Coey, M. Venkatesan, C.B. Fitzgerald, Donor impurity band exchange in dilute ferromagnetic oxides, Nat. Mater. 4 (2005) 173–179.

[10] C.H. Xia, C.G. Hu, P. Chen, B.Y. Wan, X.S. He, Y.S. Tian, Magnetic properties and photoabsorption of the Mn-doped CeO_2 nanords, Mater. Res. Bull. 45 (2010) 794–798.

[11] E. Tóthová, M. Senna, A. Yermakov, J. Kováč, E. Dutková, M. Hegedüs, M. Kaňuchová, M. Baláž, Z. Lukáčová Bujňáková, J. Briančin, P. Makreski, Zn-source dependent magnetic properties of undoped ZnO nanoparticles from mechanochemically derived hydrozincite, J. Alloys Compd. 787 (2019) 1249–1259.

[12] J.M.D. Coey, M. Venkatesan, P. Stamenov, C.B. Fitzgerald, L.S. Dorneles, Magnetism in hafnium dioxide, Phys. Rev. B 72 (2005), 024450.

[13] A. Sundaresan, C.N.R. Rao, Ferromagnetism as a universal feature of inorganic nanoparticles, Nano Today 4 (2009) 96–106.

[14] M.Y. Ge, E.Z. Wang, J.F. Liu, J.Z. Jiang, Y.K. Li, Z.A. Xu, H.Y. Li, On the origin of ferromagnetism in CeO_2 nanocubes, Appl. Phys. Lett. 93 (2008), 062505.

[15] V. Fernandes, R.J.O. Mossanek, P. Schio, J.J. Klein, A.J.A. de Oliviera, W.A. Ortiz, N. Mattoso, J. Varalda, W.H. Schreiner, M. Abbate, D.H. Mosca, Dilute-defect magnetism: origin of magnetism in nanocrystalline CeO_2, Phys. Rev. B 80 (2009), 035202.

[16] A.G. El Hachimi, H. Zaari, M. Boujnah, A. Benyoussef, M. El Yadari, A. El Kenz, Ferromagnetism induced by oxygen related defects in CeO_2 from first principles study, Comput. Mater. Sci. 85 (2014) 134–137.

[17] Z.S. Lu, D.W. Ma, J. Zhang, G.L. Xu, Z.X. Yang, First principles study of the magnetism driven by cation defects in CeO_2: the important role of O_{2p} states, Chin. Phys. B 21 (2012) 5.

[18] S.Y. Chen, Y.H. Lu, T.W. Huang, D.Ch Yan, ChL. Dong, Oxygen vacancy dependent magnetism of CeO_2 nanoparticles prepared by thermal decomposition method, J. Phys. Chem. C 114 (2010) 19576–19581.

[19] L. Wang, F. Meng, Oxygen vacancy and Ce^{3+} ion dependent magnetism of monocrystal CeO_2 nanopoles synthesized by a facile hydrothermal method, Mater. Res. Bull. 48 (2013) 3492–3498.

[20] Y.L. Liu, Z. Lockman, A. Aziz, J. MacManus-Driscoll, Size dependent ferromagnetism in cerium oxide (CeO_2) nanostructures independent of oxygen vacancies, J. Phys. Condens. Matter 20 (2008) 165201.

[21] M.J. Li, S.H. Ge, L. Qiao, L. Zhang, Y.L. Zuo, S.M. Yan, Relationship between the surface chemical states and magnetic properties of CeO_2 nanoparticles, Appl. Phys. Lett. 94 (2009) 152511.

[22] W. Lee, S.Y. Chen, Y.S. Chen, ChL. Dong, H.J. Lin, ChT. Chen, A.J. Gloter, Defect structure guided room temperature ferromagnetism of Y-doped CeO_2 nanoparticles, Phys. Chem. C 118 (2014) 26359–26367.

[23] K. Ackland, J.M.D. Coey, Room temperature magnetism in CeO_2 – a review, Phys. Rep. 746 (2018) 1–39.

[24] M. Fabián, B. Antić, V. Girman, M. Vucinić-Vasić, A. Kremenović, S. Suzuki, H. Hahn, V. Šepelák, Mechanosynthesis and structural characterization of nanocrystalline $Ce_{1-x}Y_xO_{2-\delta}$ (x 0.1-0.35), J. Solid State Chem. 230 (2015) 42–48.

[25] V. Matolín, M. Cabala, V. Cháb, I. Matolínová, K.C. Prince, M. Škoda, F. Šuara, T. Skála, K. Veltruská, A resonant photoelectron spectroscopy study of $Sn(O_x)$ doped CeO_2 catalysts, Surf. Interface Anal. 40 (2008) 225–230.

[26] E.J. Preisler, O.J. Marsh, R.A. Beach, T.C. McGill, Stability of cerium oxide on silicon studied by x-ray photoelectron spectroscopy, J. Vac. Sci. Technol. B 19 (2001) 1611–1618.

[27] P. Druska, U. Steinike, V. Šepelák, Surface structure of mechanically activated and of mechanosynthesized zinc ferrite, J. Solid State Chem. 146 (1999) 13–21.

[28] S. Aškrabić, Z.D. Dohčević-Mirović, V.D. Araújo, G. Ionita, M.M. de Lima Jr., A. Cantarero, F-centre luminescence in nanocrystalline CeO_2, J. Phys. D Appl. Phys. 46 (2013) 495306.

[29] D. Kubelka, L. Munk, Ein Beitrag Zur Optik der Farbanstriche, Z. Tech. Physik 12 (1931) 593–601.

[30] F. Goubin, X. Rocquefelte, M.H. Whangbo, Y. Montardi, R. Brec, S. Jobic, Experimental and theoretical characterization of the optical properties of CeO_2, $SrCeO_3$, and Sr_2CeO_4 containing Ce^{4+} (f^0) ions, Chem. Mater. 16 (2004) 662–669.

[31] F. Cheviré, F. Munoz, ChF. Baker, F. Tessier, O. Larcher, S. Boujday, Ch Colbeau-Justin, R. Marchand, UV absorption properties of ceria-modified compositions within the fluorite-type solid solution $CeO_2 – Y_6WO_{12}$, J. Solid State Chem. 179 (2006) 3184–3190.

[32] L. Li, F. Chen, J.Q. Lu, M.F. Luo, Study of defect sites in Ce1-xMxO2-δ (x 0.2) solid solutions using Raman spectroscopy, J. Phys. Chem. A 115 (2011) 7972–7977.

[33] S. Suzuki, I. Kosacki, V. Petrovsky, H.U. Anderson, Optical properties of undoped and Gd-doped CeO_2 nanocrystalline thin films, J. Appl. Phys. 91 (2002) 2308–2314.

[34] S.H. Yu, H. Colfen, A. Fischer, High quality CeO_2 nanocrystals stabilized by a double hydrophilic block copolymer, Colloid. Surface. 243 (2004) 49–52.

[35] S. Sathyamurthy, K.J. Leonard, R.T. Dabestani, M.P. Paranthaman, Reverse micellar synthesis of cerium oxide nanoparticles, Nanotechnology 16 (2005) 1960–1964.

[36] S. Maensiri, Ch Masingboon, P. Laokul, W. Jareonboon, V. Promarak, P. L. Anderson, S. Seraphins, Egg white synthesis and photoluminescence of platelike clusters of CeO_2 nanoparticles, Cryst. Growth Des. 7 (2007) 950–955.

[37] A. Bensalem, J.C. Muller, F. Bozon-Verduraz, Faraday Communications. From bulk CeO_2 to supported cerium-oxygen clusters: a diffuse reflectance approach, J. Chem. Soc. Faraday. Trans. 88 (1992) 153–154.

[38] S. Tsunekawa, T. Fukuda, A. Kasuya, Blue shift in ultraviolet spectra of monodisperse CeO_{2-x} nanoparticles, J. Appl. Phys. 87 (2000) 1318–1321.

[39] K.Q. Liu, M.Q. Zhong, Y.Q. Shi, Synthesis and characterization of stable and crystalline $Ce_{0.6}Y_{0.4}O_{1.8}$ nanoparticle sol, Mater. Sci. Eng. B 176 (2011) 157–162.

[40] N.V. Skorodumova, R. Ahuja, S.I. Simak, I.A. Abrikosov, B. Johansson, B. I. Lundqvist, Electronic, bonding, and optical properties of CeO_2 and Ce_2O_3 from first principles, Phys. Rev. B 64 (2001) 1151081–1151089.

[41] M. Radović, Z. Dohčević-Mitrović, A. Golubović, V. Fruth, S. Preda, M. Šćepanović, Z.V. Popović, Influence of Fe^{3+}-doping on optical properties of CeO_{2-y} nanopowders, Ceram. Int. 39 (2013) 4929–4936.

[42] T. Masui, K. Fujiwara, K. Machida, G. Adachi, T. Sakata, M. Hiratoro, Characterization of cerium (IV) oxide ultrafine particles prepared using reversed micelles, Chem. Mater. 9 (1997) 2197–2204.

[43] Z. Wang, Z. Quan, J. Lin, Remarkable changes in the optical properties of CeO_2 nanocrystals induced by lanthanide ions doping, Inorg. Chem. 46 (2007) 5237–5242.

[44] L. Yin, Y. Wang, G. Pang, Y. Koltypin, A. Gedanken, Sonochemical synthesis of cerium nanoparticles-Effect of additivies on quantum size effect, J. Colloid Interface Sci. 246 (2002) 78–84.

[45] B. Tatar, E.D. Sam, K. Kultu, M. Ürgen, Synthesis and optical properties of CeO_2 nanocrystalline films grown by pulsed electron beam deposition, J. Mater. Sci. 43 (2008) 5102–5108.

[46] M. Guo, J. Lu, Y. Wu, Y. Wang, M. Luo, UV and visible Raman studies of oxygen vacancies in rare-earth-doped ceria, Langmuir 27 (2011) 3872–3877.

[47] M.J. Li, Z.C. Feng, G. Xiong, P.L. Ying, Q. Xin, C. Li, Phase transformation in the surface region of zirconia detected by UV Raman spectroscopy, J. Phys. Chem. B 105 (2001) 8107–8111.

[48] J.C. Conesa, Computer modeling of surfaces and defects on cerium oxide, Surf. Sci. 339 (1995) 337–352.

[49] J.M.D. Coey, K. Wongsaprom, J. Alaria, M. Venkatesan, Charge-transfer ferromagnetism in oxide nanoparticles, J. Phys. D Appl. Phys. 41 (2008) 134012.

[50] B. Zhou, S. Dong, H. Zhao, P. Wu, Effects of electronic modification and structural distortion on ferromagnetism in sputtered CeO_2 films with isovalent Sn^{4+} doping, RSC Adv. 4 (2014) 63228–63233.

[51] X. Chen, G. Li, Y. Su, X. Qiu, L. Li, Z. Zou, Synthesis and room-temperature ferromagnetism of CeO_2 nanocrystals with nonmagnetic Ca^{2+} doping, Nanotechnology 20 (2009) 115606.

[52] J. Ibanez-Azpiroz, M. dos Santos Dias, S. Blügel, S. Lounis, Spin-fluctuation and spin-relaxation effects of single adatoms from first principles, J. Phys. Condens. Matter 30 (2018) 343002.

[53] P. Crespo, P. de la Presa, M. Marín, M. Multigner, J.M. Alonso, G. Rivero, F. Yndurian, J.M. González-Calbert, A. Hernando, Magnetism in nanoparticles: Tuning properties with coatings, J. Phys. Condens. Matter 25 (2013) 484006.

[54] D.M. Edwards, M.I. Katsnelson, High-temperature ferromagnetism of sp electrons in narrow impurity bands, Application to CaB_6, J. Phys. Condens. Matter 18 (2006) 7209.

[55] G.Z. Xing, Y.H. Lu, Y.F. Tian, J.B. Yi, C.C. Lim, G.P. Li, D.D. Wang, B. Yao, J. Ding, Y.P. Feng, T. Wu, Defect-induced magnetism in undoped wide band gap oxides: zinc vacancies in ZnO as an example, AIP Adv. 1 (2011), 022152.